JACS
JOURNAL OF THE AMERICAN CHEMICAL SOCIETY
Article
pubs.acs.org/JACS

Sulfur K-edge X-ray Absorption Spectroscopy and Time-Dependent Density Functional Theory of Dithiophosphinate Extractants: Minor Actinide Selectivity and Electronic Structure Correlations

Scott R. Daly, Jason M. Keith, Enrique R. Batista,* Kevin S. Boland, David L. Clark, Stosh A. Kozimor,* and Richard L. Martin

Los Alamos National Laboratory, Los Alamos, New Mexico 87545, United States

Supporting Information

ABSTRACT: The dithiophosphinic acid $HS_2P(o\text{-}CF_3C_6H_4)_2$ is known to exhibit exceptionally high extraction selectivities for trivalent minor actinides (Am and Cm) in the presence of trivalent lanthanides. To generate insight that may account for this observation, a series of $[PPh_4][S_2PR_2]$ complexes, where R = Me (**1**), Ph (**2**), *p*-$CF_3C_6H_4$ (**3**), *m*-$CF_3C_6H_4$ (**4**), *o*-$CF_3C_6H_4$ (**5**), *o*-MeC_6H_4 (**6**), and *o*-$MeOC_6H_4$ (**7**), have been investigated using sulfur K-edge X-ray absorption spectroscopy (XAS) and time-dependent density functional theory (TDDFT). The experimental analyses show distinct features in the spectrum of $S_2P(o\text{-}CF_3C_6H_4)_2^-$ (**5**) that are not present in the spectrum of **4**, whose conjugate acid exhibits reduced selectivity, or in the spectra of **2** and **3**, which are anticipated to have even lower separation factors based on previous studies. In contrast, the spectrum of **5** is similar to those of **6** and **7**, despite the significantly different electron-donating properties associated with the *o*-CF_3, *o*-Me, and *o*-OMe substituents. The TDDFT calculations suggest that the distinct spectral features of **5**−**7** result from steric interactions due to the presence of the ortho substituents, which force the aryl groups to rotate around the P−C bonds and reduce the molecular symmetry from approximately C_{2v} in **2**−**4** to C_2 in **5**−**7**. As a consequence, the change in aryl group orientation appears to make the ortho-substituted $S_2PR_2^-$ anions "softer" extractants compared with analogous Ph-, *p*-$CF_3C_6H_4$-, and *m*-$CF_3C_6H_4$-containing ligands (**2**−**4**) by raising the energies of the sulfur valence orbitals and enhancing orbital mixing between the S_2P molecular orbitals and the aryl groups bound to phosphorus. Overall, we report that sulfur K-edge XAS experiments and TDDFT calculations reveal unique electronic properties of the $S_2P(o\text{-}CF_3C_6H_4)_2^-$ anion in **5**. These results correlate with the special extraction properties associated with $HS_2P(o\text{-}CF_3C_6H_4)_2$, and suggest that ligand K-edge XAS and TDDFT can be used to guide separation efforts relevant to advanced fuel cycle development.

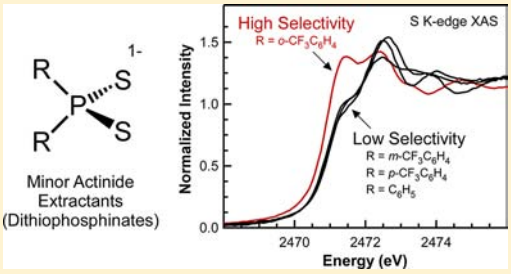

INTRODUCTION

One of the most difficult chemical problems associated with the implementation of advanced nuclear fuel cycles is the separation of trivalent minor actinides (americium and curium) from trivalent lanthanides.[1−4] These 4f and 5f elements are difficult to separate because they have similar chemical and physical properties.[1] It has been found that certain soft-donor ligands are exceptional for removing trivalent minor actinides from lanthanides via liquid/liquid extraction,[5−19] but the factors that influence this selectivity are not well understood. While there are many variables that contribute to effective separations,[20] it has long been proposed that soft-donor ligands are successful because of enhanced covalent metal−ligand bonding with actinides relative to lanthanides.[1,21,22] Despite significant advances in the development of minor actinide/lanthanide separation methods,[23−28] quantifying the role that electronic structure and covalency play in liquid/liquid extraction processes remains a grand challenge in actinide chemistry.[22]

Presented here is a ligand K-edge X-ray absorption spectroscopy (XAS) and time-dependent density functional theory (TDDFT) study that correlates electronic structure and bonding trends associated with the extractants' ability to separate actinides and lanthanides. Although these techniques are now routinely used to quantify covalency in inorganic and bioinorganic systems,[29−70] they have not been employed previously in separation science. Here we focus on sulfur donor extractants known as dithiophosphinic acids (HS_2PR_2) because they exhibit some of the highest minor actinide/lanthanide separation factors (SFs) known to date. For instance, bis(2,4,4-trimethylpentyl)dithiophosphinic acid, known commercially as Cyanex 301, yields separation factors of >5000 for americium over europium.[7] Even more impressive are the dithiophosphinic acids that contain CF_3 substituents on the aryl groups attached to phosphorus; an exceptionally high separation factor of 100 000 has been reported for ortho-substituted $HS_2P(o\text{-}CF_3C_6H_4)_2$.[71] The performance of HS_2PR_2 is dramatically affected by subtle changes in the positioning of the CF_3 substituents on the aryl backbone, as shown in Scheme

Received: April 26, 2012
Published: August 24, 2012

   dx.doi.org/10.1021/ja303999q | J. Am. Chem. Soc. 2012, 134, 14408−14422

Scheme 1. Americium/Europium Separation Factors ($SF_{Am/Eu}$) for Selected CF_3-Substituted Diaryldithiophosphinic Acids[71,72]

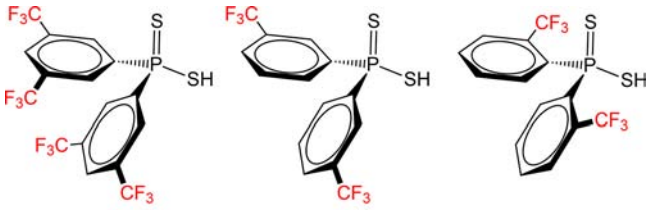

1. It has been reported that the separation factor decreases from 100 000 to 1000 when R = *m*-$CF_3C_6H_4$ and drops even further when R = (*m*-CF_3)$_2C_6H_3$ (SF = 20).[72] Separation factors for the para derivative (R = *p*-$CF_3C_6H_4$) are expected to be similarly low but have yet to be reported, and the separation factor for CF_3-free HS_2PPh_2 has been measured to be only 10, albeit using a different organic diluent.[15] Hence, these dithiophosphinic acids are attractive candidates for identifying electronic structure and reactivity correlations because they exhibit selectivities that range from highly effective to ineffective.

In this work, to provide new insight into how the ancillary groups attached to phosphorus affect the electronic structure and bonding in dithiophosphinate extractants, a series of well-defined $[PPh_4][S_2PR_2]$ complexes **1**−**7** (Figure 1) were

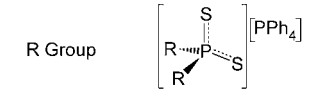

R Group	
Methyl (Me)	(**1**)
Phenyl (Ph)	(**2**)
p-$CF_3C_6H_4$	(**3**)
m-$CF_3C_6H_4$	(**4**)
o-$CF_3C_6H_4$	(**5**)
o-MeC_6H_4	(**6**)
o-$MeOC_6H_4$	(**7**)

Figure 1. Numbering convention used for $[PPh_4][S_2PR_2]$ complexes.

analyzed using sulfur K-edge XAS and TDDFT. The PPh_4^+ salts were used because the sulfur atoms are in equivalent chemical environments and free of any intermolecular cationic interactions.[73] The series also provides systematically varied ancillary groups attached to phosphorus that allowed inductive effects on the P−S interaction to be characterized using sulfur K-edge XAS. For example, when R = Me, the electronic contributions to the P−S bonding from the methyl groups are limited primarily to C−P σ interactions. Subsequent comparison of $S_2PMe_2^-$ with $S_2PPh_2^-$ allowed transitions associated with the π interactions from the phenyl groups to be unambiguously identified, thereby providing a foundation for interpreting more complicated interactions associated with the substituted aryl groups shown in Figure 1. This methodical approach enabled us to evaluate P−S orbital mixing as a function of (1) the position of the CF_3 substituent on the aryl group (ortho, meta, para) and (2) the electron-donating ability of the substituent at the ortho position (CF_3, Me, MeO). In addition, we present these results in comparison with previously reported extraction data and discuss correlations relevant for future innovation in actinide/lanthanide separation science.

RESULTS AND DISCUSSION

Sulfur K-Edge XAS Spectra. The normalized and background-subtracted sulfur K-edge X-ray absorption spectra for $[PPh_4][S_2PR_2]$ complexes **1**− **7** encapsulated in polystyrene are provided in Figure 2. The spectra have been truncated to

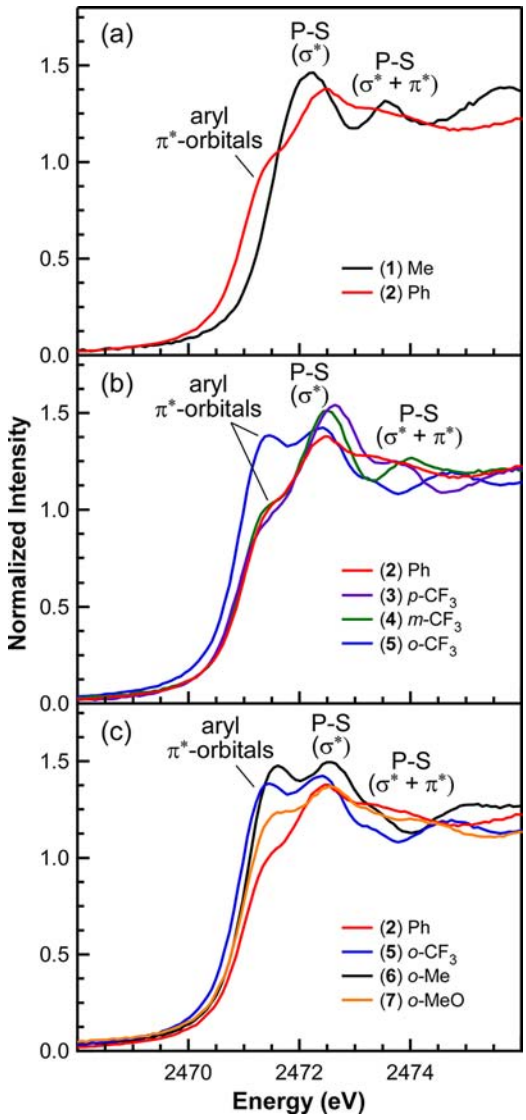

Figure 2. Comparison of the sulfur K-edge X-ray absorption spectra of **1**−**7**. The spectrum of $S_2PPh_2^-$ (**2**, red) is compared with those of (a) $S_2PMe_2^-$ (**1**, black); (b) CF_3-substituted diaryldithiophosphinates $S_2P(p\text{-}CF_3C_6H_4)_2^-$ (**3**, purple), $S_2P(m\text{-}CF_3C_6H_4)_2^-$ (**4**, green), and $S_2P(o\text{-}CF_3C_6H_4)_2^-$ (**5**, blue); and (c) ortho-substituted diaryldithiophosphinates $S_2P(o\text{-}CF_3C_6H_4)_2^-$ (**5**, blue), $S_2P(o\text{-}MeC_6H_4)_2^-$ (**6**, black), and $S_2P(o\text{-}MeOC_6H_4)_2^-$ (**7**, orange).

focus on the pre-edge regions (2468−2476 eV). To provide a quantitative comparison of peak positions and amplitudes, the spectra were modeled using pseudo-Voigt functions with Lorentzian and Gaussian ratios fixed at 1:1 and a step function with a 1:1 ratio of arctangent and error function contributions. Figures 3 and 4 show the modeling results for the pre-edge regions of the spectra, and the complete fits are provided in the Supporting Information. In each model, a best fit was obtained

dx.doi.org/10.1021/ja303999q | J. Am. Chem. Soc. 2012, 134, 14408−14422

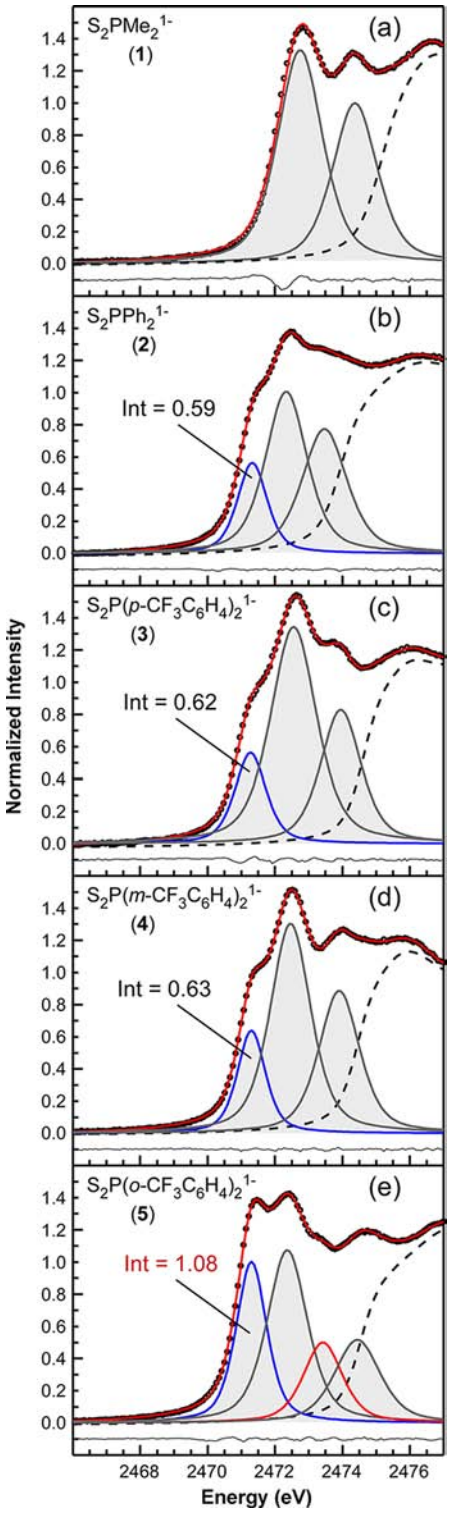

Figure 3. Sulfur K-edge X-ray absorption spectra of (a) $S_2PMe_2^-$ (**1**), (b) $S_2PPh_2^-$ (**2**), (c) $S_2P(p\text{-}CF_3C_6H_4)_2^-$ (**3**), (d) $S_2P(m\text{-}CF_3C_6H_4)_2^-$ (**4**), and (e) $S_2P(o\text{-}CF_3C_6H_4)_2^-$ (**5**) with curve-fitting analysis. Each experimental spectrum is represented as black circles, with the corresponding model overlaid as a red trace. The pre-edge functions used to generate each model are shown (gray pseudo-Voigt functions with red, blue, and black traces), as well as the post-edge residual (dashed line). The least-squares residual for each fit is represented by the gray line at the bottom of the corresponding panel.

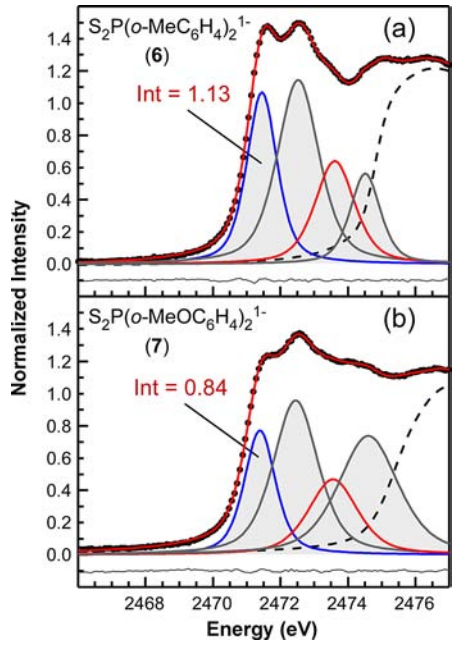

Figure 4. Sulfur K-edge X-ray absorption spectra of (a) $S_2P(o\text{-}MeC_6H_4)_2^-$ (**6**) and (b) $S_2P(o\text{-}MeOC_6H_4)_2^-$ (**7**) with curve-fitting analysis. Each experimental spectrum is represented as black circles, with the corresponding model overlaid as a red trace. The pre-edge functions used to generate each model are shown (gray pseudo-Voigt functions with red, blue, and black traces), as well as the post-edge residual (dashed line). The least-squares residual for each fit is represented by the gray line at the bottom of the corresponding panel.

when the step function was refined between 2474 and 2475 eV. The modeled pre-edge peak positions (Table 1) closely match those determined from the first- and second-derivative traces, varying in most cases by less than 0.02 eV. While the energy of

Table 1. Experimental and TDDFT-Calculated Sulfur K-Edge XAS Peak Positions

compound	curve fit (eV)	TDDFT (eV)
$S_2PMe_2^-$ (**1**)	2472.13	2472.22
	2473.61	2473.80
$S_2PPh_2^-$ (**2**)	2471.32	2472.13
	2472.33	2472.55
	2473.46	2473.95
$S_2P(p\text{-}CF_3C_6H_4)_2^-$ (**3**)	2471.27	2471.77
	2472.55	2472.51
	2473.95	2473.87
$S_2P(m\text{-}CF_3C_6H_4)_2^-$ (**4**)	2471.30	2470.94
	2472.46	2472.54
	2473.90	2473.88
$S_2P(o\text{-}CF_3C_6H_4)_2^-$ (**5**)	2471.29	2471.11
	2472.38	2472.34
	2473.42	2473.02
	2474.36	2474.00
$S_2P(o\text{-}MeC_6H_4)_2^-$ (**6**)	2471.45	2471.32
	2472.52	2472.59
	2473.61	2473.60
	2474.51	2474.15
$S_2P(o\text{-}MeOC_6H_4)_2^-$ (**7**)	2471.39	2471.41
	2472.45	2472.56
	2473.56	2473.60
	2474.60	2474.16

dx.doi.org/10.1021/ja303999q | J. Am. Chem. Soc. 2012, 134, 14408−14422

Table 2. Comparison of Calculated Bond Distances and Angles for $S_2PR_2^-$ Complexes[a]

complex	S−P (Å)	P−C (Å)	S−P−S (deg)	C−P−C (deg)	C−P−S (deg)	θ (deg)[b]
$S_2PMe_2^-$ (**1**)	2.023	1.859	122.07	100.57	108.0/108.0	–
$S_2PPh_2^-$ (**2**)	2.016	1.876	121.39	99.22	108.5/108.5	5.6
	[1.976(1)]	[1.832(3)]	[118.13(4)]	[103.5(1)]		[21.8]
$S_2P(p\text{-}CF_3C_6H_4)_2^-$ (**3**)	2.010	1.879	122.10	98.69	108.2/108.6	13.5
$S_2P(m\text{-}CF_3C_6H_4)_2^-$ (**4**)	2.010	1.879	122.24	98.88	108.3/108.3	6.1
$S_2P(o\text{-}CF_3C_6H_4)_2^-$ (**5**)	2.011	1.902	119.39	109.25	104.2/109.8	45.2
	[1.983(2)]	[1.860(6)]	[116.46(8)]	[111.0(2)]	[104.2(2)/110.4(2)]	[52.5]
					[104.2(2)/110.8(2)]	
$S_2P(o\text{-}MeC_6H_4)_2^-$ (**6**)	2.021	1.880	118.41	103.47	107.2/109.8	45.3
	[1.992(2)]	[1.838(3)]	[117.25(4)]	[106.9(1)]	[105.78(8)/108.95(8)]	[52.2]
					[107.41(8)/110.10(8)]	
$S_2P(o\text{-}MeOC_6H_4)_2^-$ (**7**)	2.022	1.867	118.14	104.11	107.6/109.3	49.0
	[1.989(2)]	[1.836(4)]	[115.65(5)]	[104.4(1)]	[108.4(1)/109.4(1)]	[46.2]
					[109.1(1)/109.4(1)]	

[a]Values in brackets represent experimental values from the reported crystallographic data for $[PPh_4][S_2PR_2]$ complexes.[73] The experimental bond lengths and θ angles represent average values. [b]For the definition of θ, see Scheme 2.

these features could be determined with high confidence, the overall intensities for many of the pre-edge features at higher energy (>2472 eV) varied significantly because of substantial overlap with adjacent features. In addition, because of a small but systematic contribution to the post-edge regions of the spectra (>2480 eV) from a sulfate contaminant in the polystyrene, only the relative intensity of the first pre-edge feature in each spectrum will be discussed (estimated error ≤5%).

To facilitate the identification of spectral differences for **1**−**7**, our discussion of the data will follow a general outline that begins with the comparatively simple $S_2PMe_2^-$ ion, then moves to the more complicated $S_2PPh_2^-$ ion, and finally describes diaryldithiophosphinates that contain CF_3, Me, or MeO substituents. It is instructive to first consider $S_2PMe_2^-$ (**1**) because it is highly symmetric (C_{2v}) and the P−C interactions are dominated by σ bonding. Comparison of $S_2PMe_2^-$ with $S_2PPh_2^-$ (**2**) allows the effects of P−C π conjugation to be evaluated because both P−C σ and π bonding interactions are present in $S_2PPh_2^-$. Combined, the analyses of **1** and **2** provide a foundation to interpret the sulfur K-edge XAS spectra of **3**−**7** and enable us to characterize the effects of symmetry and substituents on the sulfur K-edge XAS spectra of CF_3-, Me-, and MeO-substituted diaryldithiophosphinates.

The spectrum of methyl-containing **1** is best modeled by two intense and well-resolved pre-edge features at 2472.13 and 2473.61 eV (Figures 2a and 3a). At intermediate energy (ca. 2475.7 eV), there is an additional broad feature that is not fully resolved from higher-energy features and the onset of the rising edge. Figure 2a shows the effect of replacing the methyl group (black) with a phenyl group (red). As observed for **1**, the spectrum of **2** also contains two pre-edge features at 2472.33 and 2473.46 eV, although they are less resolved from the higher-energy peaks. Another subtle variation between the two spectra is associated with the line shape for the high-energy residual (dashed line in Figure 3b), which for **2** is broadened and shifted to slightly lower energy. The most pronounced difference is that the $S_2PPh_2^-$ spectrum contains a low-energy pre-edge shoulder at 2471.32 eV, which appears to result from phenyl π-orbital mixing with the S_2P orbitals, since analogous π interactions are not present in $S_2PMe_2^-$.

Figure 2b shows the effect of introducing CF_3 substituents on the aryl groups by comparing the sulfur K-edge XAS spectra of $S_2PPh_2^-$ (**2**; red) to $S_2P(p\text{-}CF_3C_6H_4)_2^-$ (**3**; purple), $S_2P(m\text{-}CF_3C_6H_4)_2^-$ (**4**; green), and $S_2P(o\text{-}CF_3C_6H_4)_2^-$ (**5**; blue). The spectra of **2**−**4** can be described, in general, as having a low-energy pre-edge shoulder near 2471.3 eV and two higher-energy pre-edge features near 2472 and 2474 eV. For $S_2P(p\text{-}CF_3C_6H_4)_2^-$ (**3**) and $S_2P(m\text{-}CF_3C_6H_4)_2^-$ (**4**), which contain CF_3 substituents at the para and meta positions, respectively, the pre-edge shoulders are small and can be superimposed on that of **2**. Curve-fitting analysis shows these features have identical peak energies and intensities within experimental error (Figure 3b−d and Table 1). In contrast, the pre-edge shoulder for $S_2P(o\text{-}CF_3C_6H_4)_2^-$ (**5**), which contains o-CF_3 substituents, is slightly lower in energy (ca. 0.2 eV), better resolved, and nearly twice as intense as the shoulders for **2**−**4** (Figure 3e and Table 1). In addition, the curve-fitting analysis reveals that the third feature observed in the spectra of **2**−**4** near 2474 eV has split into two features located at 2473.42 and 2474.36 eV in the spectrum of **5**.

To evaluate the origin of the large pre-edge feature observed for ortho-substituted **5**, $[PPh_4][S_2PR_2]$ salts containing the anions $S_2P(o\text{-}MeC_6H_4)_2^-$ (**6**) and $S_2P(o\text{-}MeOC_6H_4)_2^-$ (**7**) were analyzed, and Figure 2c compares their pre-edge regions to those of $S_2P(o\text{-}CF_3C_6H_4)_2^-$ (**5**; blue) and $S_2PPh_2^-$ (**2**; red) for reference. Within this series, the ability of the ancillary aryl group to donate electron density to the S_2P core systematically increases in the order o-$CF_3C_6H_4$ < C_6H_5 < o-MeC_6H_4 < o-$MeOC_6H_4$. Consistent with this systematic electronic difference, the energies of the three pre-edge features for **6** and **7** are shifted to energies that are 0.1−0.2 eV higher than in **5** (Table 1). However, the pre-edge shoulder intensities and overall spectra of **6** and **7** are more similar to those of **5** than those of **2**. Based on this observation, the arene-containing compounds **2**−**7** can be separated into two general classes of compounds: one with low-intensity pre-edge shoulders [0.59(3), 0.62(3), and 0.63(3) for **2**−**4**, in which R = Ph, p-$CF_3C_6H_4$, and m-$CF_3C_6H_4$, respectively] and the other with significantly larger pre-edge shoulder intensities (0.84−1.13 for **5**−**7**). It is noteworthy that each member in this second class of compounds has a substituent at the ortho position of the aryl group and that the intensity of the pre-edge shoulder increases in the order o-MeO [0.84(4)] < o-CF_3 [1.08(6)] < o-Me [1.13(6)].

Calculated $S_2PR_2^-$ Structures. DFT calculations were performed to gain additional insight into the origin of the pre-edge features in the sulfur K-edge XAS spectra of **1**−**7**. The calculated structures of **2** and **5**−**7** are in close agreement with the previously reported solid-state structures,[73] thereby providing confidence in the calculated metrics for **1**, **3**, and **4**, whose structures have not yet been determined experimentally (Table 2). Both theory and experiment suggest that the bond distances and angles vary only slightly for **1**−**7**. For example, the average P−S bond distance for **1**−**7** was calculated to be 2.016 Å with a standard deviation from the mean (σ) of only 0.006 Å. Similar experimental values have been reported, and the average P−S distance for **2** and **5**−**7** is 1.985 Å (σ = 0.009 Å). As discussed previously,[73] the experimental data show that the S−P−S angles decrease and the C−P−C angles increase systematically with increasing steric bulk of the ancillary aryl group. Another consequence of the increased steric bulk is the variation of the S−P−C bond angles in the ortho-substituted complexes **5**−**7**. The variation between these angles is most pronounced for **5** (*o*-CF_3; 5.6°) and decreases sequentially for **6** (*o*-Me; 2.6°) and **7** (*o*-MeO; 1.7°). In comparison, the S−P−C bond angles are identical for **2**−**4**, and all of the calculated bond angles are consistent with those observed experimentally (Table 2). The most profound structural distortions are associated with the angle θ, which has been used previously to quantify the rotation of the aryl groups; θ is defined as the angle between the C−P−C plane and the plane defined by the aryl carbon atoms (θ = 0 when the planes are orthogonal; Scheme 2).[73] The calculated θ values for **2**−**4**, which contain

Scheme 2. Definition of the Angle θ Used To Compare Aryl Group Rotations[73]

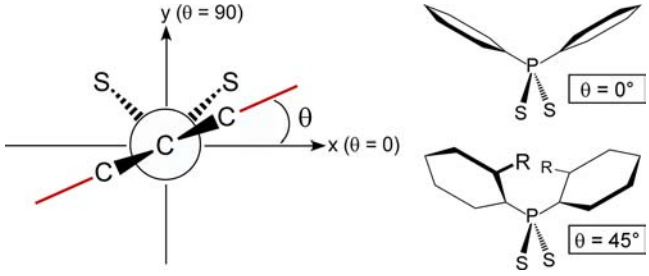

only hydrogen at the ortho positions, are all close to 0° (5.6°, 13.5°, and 6.1°, respectively) and their point groups are approximately C_{2v} if the positions of the *m*-CF_3 substituents in **4** are ignored (see below for justification). In contrast, θ approaches 45° for compounds **5**−**7**, whose arene rings have *o*-CF_3, *o*-Me, and *o*-MeO substituents (45.2°, 45.3°, and 49.0°, respectively). These calculated values are in good agreement with the average experimental θ values of 52.5°, 52.2°, and 46.2° determined for **5**−**7**. In contrast, the average experimental θ value of 21.8° for **2** is different from the theoretical value (θ = 5.6°), but both are appreciably less than those observed for **5**−**7**.[73] Overall, the experimental and calculated data suggest that steric repulsions between the ortho substituents on the aryl group and the sulfur atoms bound to phosphorus force the aryl groups to rotate around the P−C bond in **5**−**7**, as suggested previously.[74,75]

Molecular Orbital Correlation Diagrams. Since sulfur K-edge XAS probes bound-state transitions and involves dipole-allowed excitations of sulfur 1s electrons into vacant molecular orbitals (MOs) that contain some sulfur 3p character due to S−P orbital mixing,[68] MO correlation diagrams were prepared to guide the interpretation of the XAS data. Before the evaluation of how the ancillary groups attached to phosphorus contribute to bonding, the orbital interactions in the S_2P^- core within a C_{2v}-symmetric $S_2PR_2^-$ anion were first considered (Figure 5).

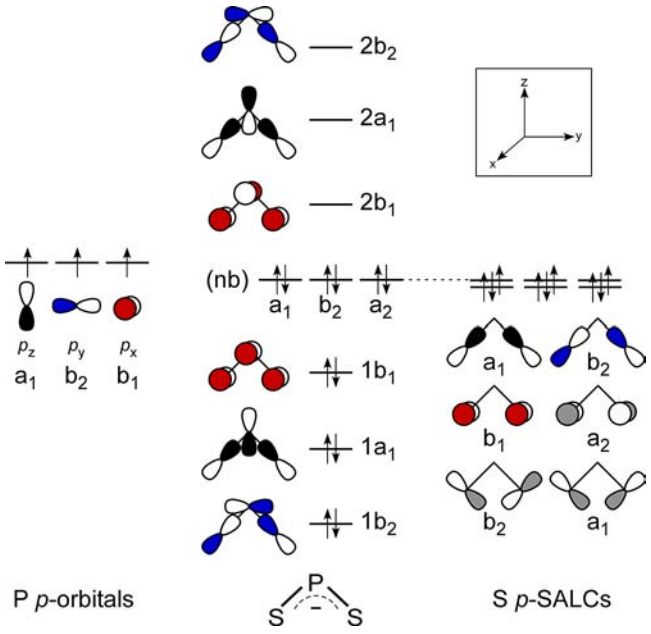

Figure 5. Qualitative MO correlation diagram of the anionic S_2P^- fragment in C_{2v} symmetry. The three nonbonding (nb) sulfur 3p SALCs are depicted as gray/white, whereas orbitals participating in bonding are shown in white with red, black, or blue.

For the S_2P^- anion, there are two σ-type symmetry-adapted linear combinations (SALCs) of sulfur 3p atomic orbitals with a_1 and b_2 symmetries that can be used to form P−S σ bonds using the two phosphorus valence 3p orbitals with those symmetries ($3p_z$ and $3p_y$, respectively). The remaining four sulfur 3p SALCs transform as $a_1 + a_2 + b_1 + b_2$. Assuming no S or P 3d orbital involvement, the a_1, a_2, and b_2 SALCs transform as the nonbonding S lone pairs, leaving only the b_1 SALC with the appropriate symmetry to form a P−S π bond with the remaining P $3p_x$ orbital.

To quantify the energies of the MOs depicted in Figure 5 and to determine how these orbitals are perturbed upon addition of σ-donor groups (Me) versus σ- and π-donating groups (aryl), DFT calculations were performed on the S_2P^-, $S_2PMe_2^-$, and $S_2PPh_2^-$ anions (Figure 6). The MO diagram for the hypothetical S_2P^- anion provided in Figure 6 is consistent with the group theory analysis in Figure 5. The addition of methyl groups in $S_2PMe_2^-$ imparts only subtle changes to the bonding picture, pushing the $3a_1$ orbital to higher energy and splitting the b_1 orbitals as a result of a three-orbital interaction due to the additional Me−P σ bonds. Replacement of the methyl groups with phenyl groups in $S_2PPh_2^-$ introduces arene−phosphorus π mixing and further splits the bonding and antibonding MOs as a result of additional three-orbital interactions. The antibonding orbitals, which are directly probed in sulfur K-edge XAS experiments, can be described as having three discrete energy regions (Figure 6). There exists a low-energy region with four orbitals that contain significant phenyl character (C−C π-antibonding) and only small contributions from sulfur and phosphorus orbitals (Table 3).

dx.doi.org/10.1021/ja303999q | J. Am. Chem. Soc. 2012, 134, 14408−14422

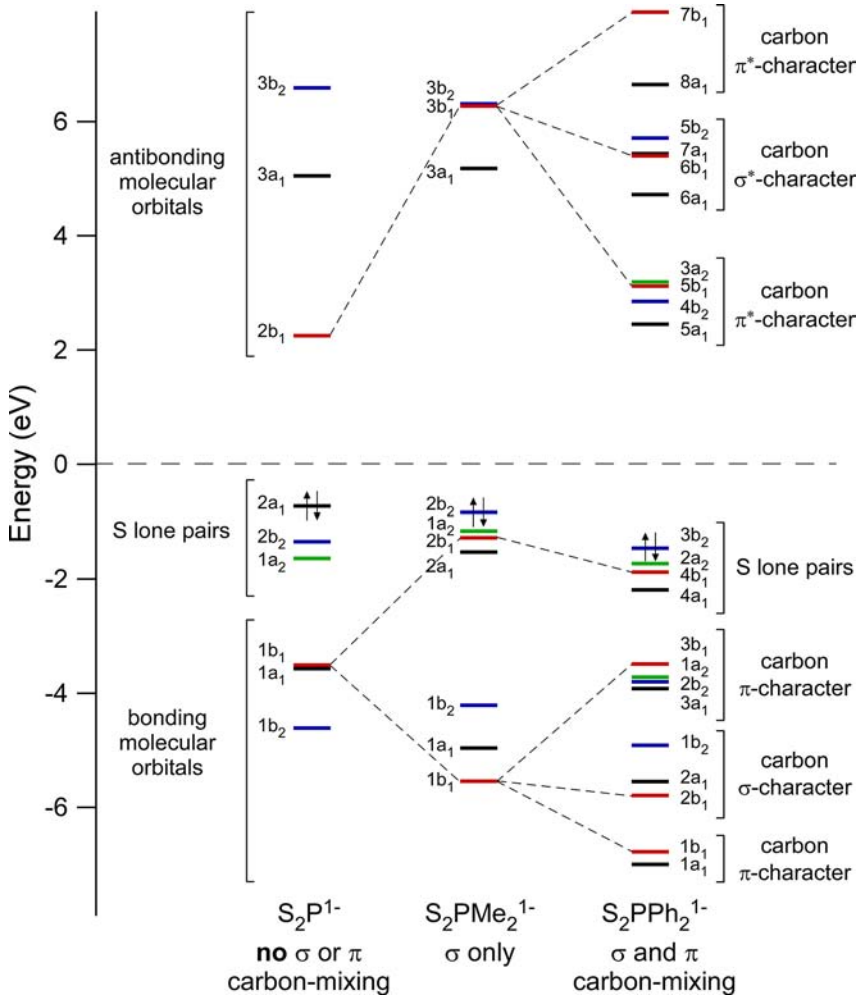

Figure 6. Calculated MO correlation diagram for the S_2P^- fragment (no groups attached to phosphorus), $S_2PMe_2^-$ (**1**), and $S_2PPh_2^-$ (**2**) showing the relative effects of carbon mixing (σ vs π) on the dithiophosphinate MOs. The MOs are color-coded to represent the symmetry labels: a_1 (black), a_2 (green), b_1 (red), and b_2 (blue).

At slightly higher energy is an intermediate group of four orbitals that are most closely related to those observed in $S_2PMe_2^-$ and contain both phenyl character (C−C σ-antibonding) and significant sulfur and phosphorus character due to S−P orbital mixing. Finally, at high energy are two additional phenyl orbitals (π-antibonding) that contain only small contributions from the S_2P unit.

The calculated MOs for **2**−**7** can all be assigned to the general regions described in Figure 6, but the energies of the orbitals in these regions are dependent primarily on changes in molecular symmetry. The approximate point groups of **2**−**7** were assigned on the basis of their experimental and calculated structures and confirmed by inspection of their Kohn−Sham orbitals. For example, the structures and Kohn−Sham orbitals clearly reflect C_{2v} symmetry for the $S_2PPh_2^-$ and $S_2P(p\text{-}CF_3C_6H_4)_2^-$ anions in **2** and **3**, respectively (Figure 7). The situation is a bit more complicated for **4** because the *m*-CF_3 substituents remove the possibility of internal mirror planes if the substituent positions are rigorously considered. Despite the prospect of lower symmetry, we found that **4** can be approximated as a C_{2v} anion on the basis of the orientation of the arene rings ($\theta \approx 0°$). The Kohn−Sham orbitals for **4** are nearly identical to those in C_{2v}-**2** and **3**, which validates the C_{2v} symmetry approximation. In contrast, similar analysis shows that the molecular symmetries of the ortho-substituted complexes **5**−**7** have been fully reduced from C_{2v} to C_2 as a result of the staggered orientation of the arene rings ($\theta \approx 45°$), and this symmetry reduction is clearly reflected in the Kohn−Sham orbitals (Figure 7). Hence, the diaryldithiophosphinates can be distinguished as those with C_{2v} symmetry (**2**−**4**) and those with C_2 symmetry (**5**−**7**).

For C_{2v}-symmetric **2**−**4**, which contain Ph, *p*-$CF_3C_6H_4$, and *m*-$CF_3C_6H_4$ groups, respectively, the first four antibonding MOs contain primarily arene carbon π^* character and have been assigned and labeled as $5a_1$, $3a_2$, $5b_1$, and $4b_2$ (Figure 8). The sulfur 3p character in these orbitals is quite low and is greater than 2% only for the orbitals with a_1 and b_1 symmetry. The differences in sulfur 3p character in these first four MOs can be rationalized in terms of orbital overlap between the π orbitals of the aryl groups and the orbitals of the S_2P fragment. As shown in Scheme 3, a conjugation pathway between the aryl rings and the S_2P unit is clearly present in the $5a_1$ and $5b_1$ orbitals, where increased sulfur 3p character is observed. In contrast, a node present at the ipso carbon of the aryl ring associated with the $3a_2$ and $4b_2$ orbitals inhibits effective conjugation of electron density between the carbon and sulfur atoms via phosphorus. Aside from the node at carbon, conjugation is further inhibited because the available

dx.doi.org/10.1021/ja303999q | J. Am. Chem. Soc. 2012, 134, 14408−14422

Table 3. Calculated $S_2PR_2^-$ Antibonding MO Energies, Compositions, and Sulfur K-Edge XAS Transitions

			DFT MO composition (%)[b]			TDDFT transition (1s → MO)		
complex	MO[a]	energy (eV)	S 3p	P 3p	C 2p	energy (eV)[c]	oscillator strength[d]	MO type
$S_2PMe_2^-$ (**1**)	$3b_2$	6.31	36.0	37.1	6.2	2473.84	0.34	S−P*
	$3b_1$	6.27	13.0	59.3	9.1	2473.77	0.36	
	$3a_1$	5.18	63.4	16.7	4.6	2472.22	1.42	
$S_2PPh_2^-$ (**2**)	$5b_2$	5.71	38.6	49.5	5.0	2473.88	0.32	S−P*
	$7a_1$	5.44	9.6	8.0	9.4	2474.22	0.12	
	$6b_1$	5.40	2.8	9.0	9.6	2474.01	0.24	
	$6a_1$	4.72	48.4	7.5	10.4	2472.55	1.08	
	$3a_2$	3.19	0.6	0	94.8	–	–	C_π*
	$5b_1$	3.12	2.2	3.4	89.4	2471.85	0.08	
	$4b_2$	2.85	0.8	1.3	93.6	–	–	
	$5a_1$	2.45	3.8	3.1	87.0	2471.10	0.24	
$S_2P(p\text{-}CF_3C_6H_4)_2^-$ (**3**)	$5b_2$	5.23	38.8	49.5	6.6	2474.01	0.32	S−P*
	$7a_1$	5.22	3.2	10.3	28.0	2474.55	0.10	
	$6b_1$	5.02	10.2	38.5	25.2	2473.93	0.32	
	$6a_1$	4.19	53.0	10.0	10.6	2472.61	1.14	
	$3a_2$	2.50	0.8	0	94.8	–	–	C_π*
	$4b_2$	2.22	0.6	0.8	91.8	–	–	
	$5b_1$	2.04	2.2	2.4	88.4	2471.44	0.08	
	$5a_1$	1.48	2.8	2.2	86.8	2470.83	0.16	
$S_2P(m\text{-}CF_3C_6H_4)_2^-$ (**4**)	$5b_2$	5.21	29.4	41.2	11.0	2473.86	0.34	S−P*
	$7a_1$	5.16	3.8	8.1	18.2	2474.27	0.10	
	$6b_1$	5.08	9.0	30.9	22.8	2473.91	0.28	
	$6a_1$	4.27	52.6	9.7	11.2	2472.54	1.12	
	$5b_1$	2.43	2.0	2.6	90.0	2471.65	0.06	C_π*
	$3a_2$	2.31	1.2	0.3	92.2	2471.57	0.06	
	$4b_2$	1.91	0.6	0.9	91.0	–	–	
	$5a_1$	1.72	3.0	2.2	88.0	2470.90	0.18	
$S_2P(o\text{-}CF_3C_6H_4)_2^-$ (**5**)	11b	5.31	7.2	8.0	8.6	2474.27	0.16	S−P*
	10a	5.13	9.6	18.2	12.4	2473.97	0.10	
	10b	4.95	23.6	47.3	8.8	2473.39	0.28	
	9a	4.45	52.4	3.7	13.8	2472.46	1.20	
	9b	2.64	2.0	1.3	92.0	2471.64	0.06	C_π*
	8a	2.53	1.0	0.2	93.0	2471.55	0.06	
	8b	2.12	3.4	2.6	86.8	2471.10	0.06	
	7a	2.05	3.4	2.7	86.1	2470.94	0.26	
$S_2P(o\text{-}MeC_6H_4)_2^-$ (**6**)	11b	5.43	22.6	34.6	15.4	2473.61	0.32	S−P*
	10a	5.36	4.0	7.8	11.4	2474.25	0.06	
	10b	5.34	8.8	22.5	7.8	2474.15	0.12	
	9a	4.75	56.1	8.6	11.8	2472.59	1.02	
	9b	3.15	0.6	0.5	93.6	–	–	C_π*
	8a	3.07	0.4	0.2	93.0	–	–	
	8b	2.82	6.0	5.3	81.6	2471.53	0.14	
	7a	2.58	4.0	3.5	85.2	2471.25	0.36	
$S_2P(o\text{-}MeOC_6H_4)_2^-$ (**7**)	11b	5.64	19.6	30.8	13.0	2473.60	0.28	S−P*
	10a	5.40	9.2	11.6	10.2	2474.14	0.06	
	10b	5.26	9.0	23.3	9.4	2474.24	0.16	
	9a	4.67	49.8	7.2	13.2	2472.56	0.94	

dx.doi.org/10.1021/ja303999q | J. Am. Chem. Soc. 2012, 134, 14408−14422

Table 3. continued

complex	MO[a]	energy (eV)	DFT MO composition (%)[b] S 3p	P 3p	C 2p	TDDFT transition (1s → MO) energy (eV)[c]	oscillator strength[d]	MO type
	9b	3.16	0.2	0.6	93.0	–	–	C_π*
	8a	3.10	1.0	0.7	91.6	2471.88	0.06	
	8b	2.91	6.2	5.4	82.2	2471.58	0.10	
	7a	2.74	3.8	2.4	87.2	2471.36	0.44	
$S_2PPh_2^-$ with rotated Ph (θ = 45°) (**2a**)	11b	5.82	24.2	41.1	11.2	2474.25	0.12	S–P*
	10a	5.37	6.6	9.4	9.6	2474.11	0.12	
	10b	5.30	4.6	12.9	8.8	2473.72	0.30	
	9a	4.79	52.6	9.1	10.0	2472.58	1.00	
	9b	3.15	0.6	0.6	94.4	2471.89	0.04	C_π*
	8a	2.89	1.0	0.0	94.4	–	–	
	8b	2.75	6.2	5.0	84.0	2471.39	0.10	
	7a	2.66	4.2	2.6	87.8	2471.23	0.40	
$S_2PPh_2^-$ at the geometry in **5** (**2b**)	11b	5.49	12.6	19.8	7.9	2474.21	0.12	S–P*
	10a	5.31	11.7	16.9	11.4	2473.95	0.08	
	10b	5.29	17.0	35.7	8.3	2473.47	0.30	
	9a	4.78	49.9	4.3	12.0	2472.54	1.12	
	9b	3.15	0.6	0.4	94.6	2471.89	0.04	C_π*
	8a	3.06	0.8	0.0	94.6	2471.80	0.04	
	8b	2.77	4.8	4.6	86.0	2471.42	0.10	
	7a	2.63	4.3	3.9	85.5	2471.22	0.32	

[a]The MO symmetry labels correspond to those used in Figures 6 and 8. [b]Only S 3p, P 3p, and C 2p contributions are given. The remaining contributions from other S, P, and C orbitals and the H, F, and O orbitals are not included. [c]The TDDFT energy values have been shifted by +57.4 eV (see the Experimental Section for details). [d]The oscillator strengths have been multiplied by a factor of 200 to bring them on scale with the experimental data in Figures 11–13.

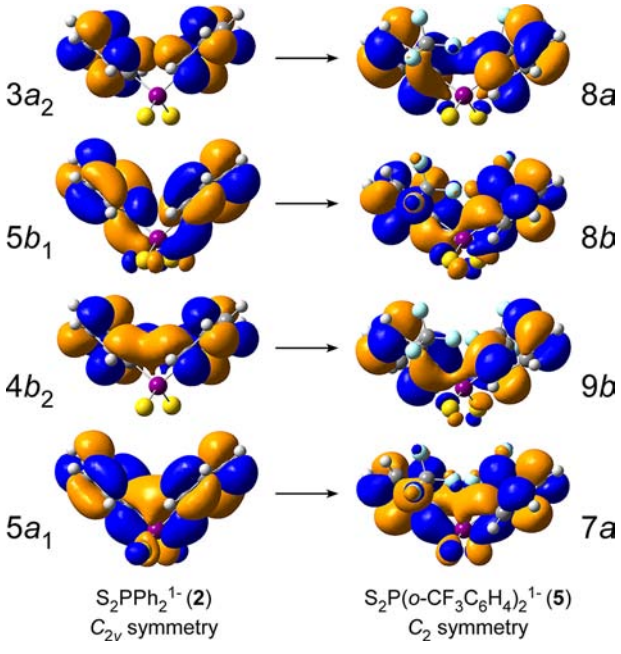

Figure 7. The first four antibonding Kohn–Sham orbitals for (left) $S_2PPh_2^-$ (**2**) and (right) $S_2P(o\text{-}CF_3C_6H_4)_2^-$ (**5**). Rotation of the aryl groups in **5** lowers the symmetry of the MOs from C_{2v} to C_2 and increases the mixing between the arene and S_2P orbitals. The labels correspond to those provided in Figures 6 and 8.

phosphorus $3p_y$ orbital having b_2 symmetry (Figure 5) is orthogonal to the b_2 aryl π orbitals (Scheme 3). Hence, there are no phosphorus 3p orbitals having a_2 and b_2 symmetry to bridge a conjugation pathway between the aryl groups and the sulfur atoms.

The reduction in symmetry from C_{2v} in **2**–**4** to C_2 in ortho-substituted **5**–**7** provides an appreciable increase in the aryl and S_2P orbital mixing. For example, the percentage of sulfur 3p character is plotted as a function of aryl group identity in Figure 9 for each of the four low-lying orbitals that are primarily C–C π* in nature. For the 8b MO (derived from $5b_1$ in C_{2v}) and 7a MO (derived from $5a_1$ in C_{2v}), moving from **2**–**4** (C_{2v}) to **5**–**7** (C_2) causes an increase in the sulfur 3p character in the 8b orbital, while the 7a orbitals are relatively unaffected. In addition, the 8b orbital energy decreases in comparison with that of 7a, as highlighted by the dashed lines in Figure 8. For almost all of the compounds analyzed (**2**–**4**, **6**, and **7**), the sulfur 3p character in the 8a and 9b orbitals (derived from $3a_2$ and $4b_2$ in C_{2v} symmetry) can be described as relatively unaffected by the aryl group identity and possess only a small percentage of sulfur 3p mixing. In contrast, the sulfur 3p character in the 9b orbital of **5** increases slightly (Figure 9). As observed in the C_{2v} anions, the decreased amount of sulfur 3p character in the 8a and 9b orbitals, particularly in **6** and **7**, is likely due to the presence of the nodes at the ipso carbon atoms, which persist despite the reduction in symmetry.

To provide insight into how the value of the angle θ (Scheme 2) affects the energy and orbital composition of the first four antibonding MOs of **2**–**7**, DFT calculations were performed on hypothetical structures of the $S_2PPh_2^-$ anion in which the phenyl groups were systematically rotated in 5° intervals from θ = 0° to θ = 45°. While the MOs of a-symmetry do not show

dx.doi.org/10.1021/ja303999q | J. Am. Chem. Soc. 2012, 134, 14408–14422

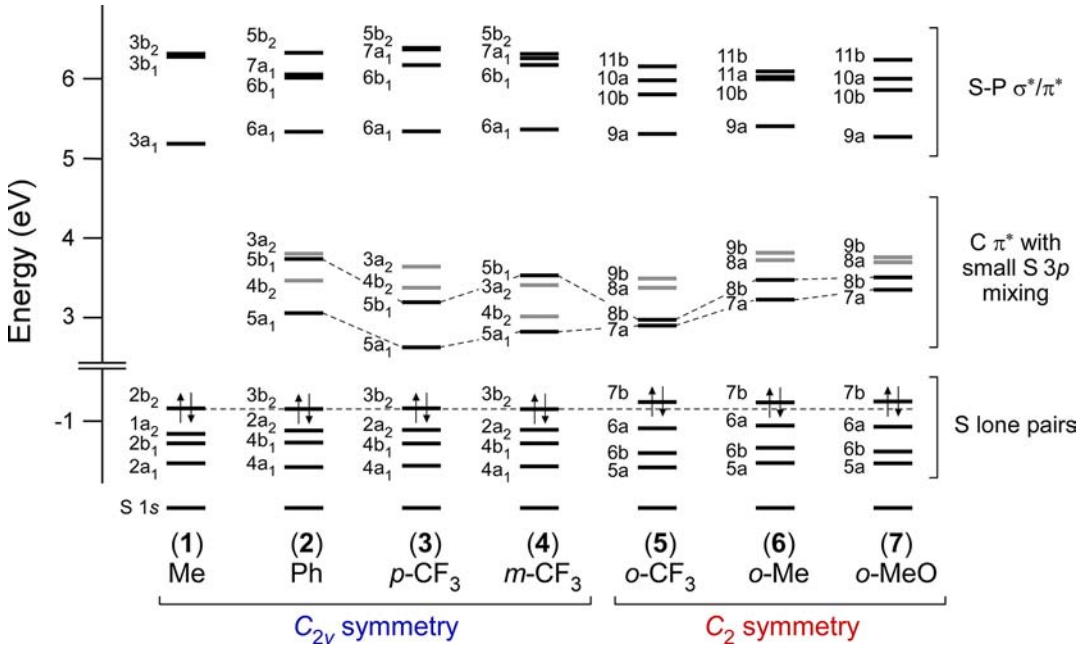

Figure 8. Truncated MO correlation diagram for **1**−**7** (left to right). The MO energies have been shifted to make the sulfur 1s orbital energies of **2**−**7** equivalent to those calculated for $S_2PMe_2^-$ (**1**). The gray bars represent MOs containing less than 2% total sulfur 3p character. The dotted lines are provided for guidance for MOs relevant to M−S bonding (S lone pairs) and for antibonding MOs relevant to the sulfur K-edge XAS spectra.

Scheme 3. Comparison of Arene Orbital Overlap in the First Four Antibonding MOs in $S_2PPh_2^-$ (2) (Symmetry Labels Correspond to Those Used in Figures 6 and 8)

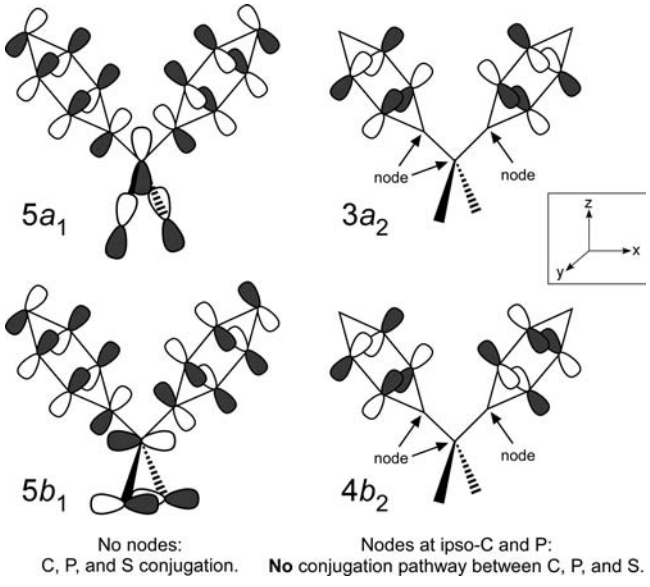

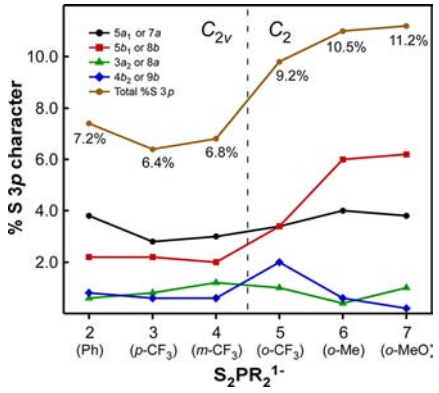

Figure 9. Comparison of the percent sulfur 3p character in the first four antibonding MOs in **2**−**7**. The labels correspond to those provided in Figures 6 and 8.

much variation corresponding to the structural change, the b_1 and b_2 orbitals transform as b-symmetric, begin to mix, and undergo an avoided crossing as the phenyl groups are rotated (Figure 10).[76] When θ reaches 45° in the theoretical structure of $S_2PPh_2^-$ (which we will call **2a**), the b orbitals of $5b_1$ and $4b_2$ parentage at θ = 0° have swapped positions. The sulfur 3p character in the 8b MO has also increased from 2.2% in the parent $4b_1$ MO in **2** to 6.2% in **2a**, which is identical to the values for C_2-symmetric **6** and **7** (6.0% and 6.2%, respectively; Table 3). Overall, the calculations reveal that the increase in total sulfur 3p character from 7.2% in **2** to 12.0% in **2a** for the first four antibonding MOs results from aryl group rotation. By extension, it appears that the increased arene group rotation from $\theta \approx 0°$ in **2**−**4** to $\theta \approx 45°$ in **5**−**7** is responsible for the increase in sulfur 3p character from 6.4−7.2% in **2**−**4** to 9.2−11.2% in **5**−**7**. The appreciable rise in sulfur 3p character in **5**−**7** can be attributed primarily to the increase in sulfur 3p character as the $5b_1$ MO is transformed into the 8b MO (Figure 9 and Table 3). If it is assumed that the first pre-edge shoulders in the experimental spectra in Figures 2 and 3 involve transitions associated with these primarily arene π^* orbitals, the calculations are in excellent agreement with the sulfur K-edge XAS data. The experimental curve fits consistently show that the first pre-edge shoulders for **5**−**7** (intensity = 0.84−1.13) are significantly larger than those in **2**−**4** (intensity = 0.59−0.63). Discussion of variations observed in the higher-energy antibonding MOs will be provided in the TDDFT section that follows.

Time-Dependent Density Functional Theory Calculations. TDDFT calculations were performed to simulate the sulfur K-edge XAS spectra of **1**−**7** and identify the transitions

dx.doi.org/10.1021/ja303999q | J. Am. Chem. Soc. 2012, 134, 14408−14422

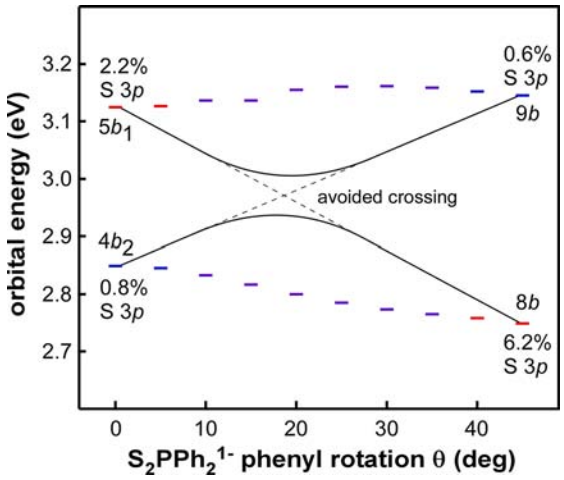

Figure 10. Walsh diagram showing the avoided crossing of the $5b_1$ and $4b_2$ MOs as the phenyl groups in $S_2PPh_2^-$ are rotated from $\theta = 0°$ to $\theta = 45°$. The labels correspond to those provided in Figure 6 and 8.

responsible for the observed features. The TDDFT results are in excellent agreement with the experimental data and are consistent with the spectral interpretations described above (Table 3). For example, the simulated sulfur K-edge XAS spectrum of $S_2PMe_2^-$ (**1**), which contains σ-donating Me groups, is shown as the dashed line in Figure 11a. It contains two features whose relative intensities, energies, and peak splitting closely match those observed in the experimental spectrum (solid line in Figure 11a). These two features correspond to three calculated transitions: the low-energy feature is assigned solely to a sulfur 1s electronic excitation to an antibonding orbital with a_1 symmetry ($3a_1$; Figures 6 and 8), while the high-energy feature contains two transitions that are close in energy and involve orbitals with b_1 and b_2 symmetry ($3b_1$ and $3b_2$; Figures 6 and 8). For comparison, the calculated TDDFT spectrum of $S_2PPh_2^-$ (**2**), which contains ancillary groups capable of mixing with the S_2P unit through both σ and π interactions, is presented in Figure 11b. The spectrum of **2** is similar to that of **1** in that it contains a feature associated with the a_1 orbital near 2472.5 eV and a high-energy feature that contains transitions involving the orbitals with b_1 and b_2 symmetry near 2474 eV ($6a_1$, $6b_1$, and $5b_2$; Figures 6 and 8). It differs in that there is an additional transition associated with the high-energy feature at 2474.22 eV involving the $7a_1$ orbital, which is best described as a C−C π^* orbital but contains small amounts of sulfur 3p character due to C_6H_5−PS_2 orbital mixing. A more obvious difference between the simulated spectra of $S_2PMe_2^-$ and $S_2PPh_2^-$ is the emergence of the low-energy pre-edge shoulder at 2472.13 eV. The calculations indicate that this feature corresponds to transitions involving the new $5a_1$ and $5b_1$ orbitals (Figures 6 and 8) that result from the new arene π conjugation with the PS_2 unit and contain only small amounts of sulfur 3p character. Overall, this is consistent with the interpretation described above.

The simulated sulfur K-edge XAS spectra of $S_2P(p\text{-}CF_3C_6H_4)_2^-$ (**3**) and $S_2P(m\text{-}CF_3C_6H_4)^-$ (**4**) are similar to the spectrum calculated for $S_2PPh_2^-$ (**2**; Figure 11b–d) and appreciably different from the simulated spectra of **5**–**7** (Figure 12). The most obvious variations are associated with the decreased energy and increased intensity observed for the first pre-edge features. More subtle changes are associated with the number of high-energy transitions near 2474 eV, and the

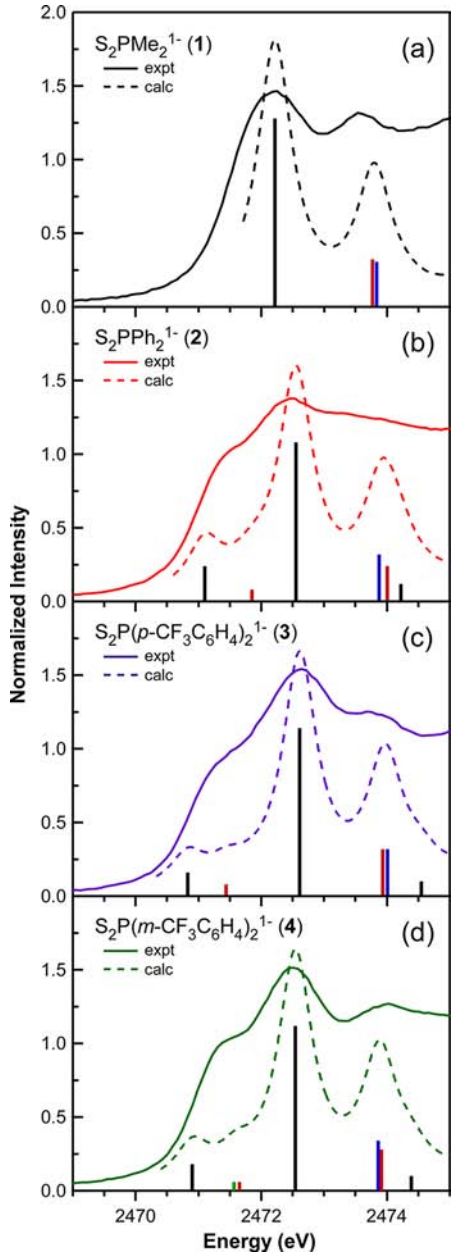

Figure 11. Sulfur K-edge X-ray absorption spectra (solid lines), TDDFT-simulated spectra (dotted lines), and calculated transitions (bars) for C_{2v}-symmetric diaryldithiophosphinates: (a) $S_2PMe_2^-$ (**1**, black); (b) $S_2PPh_2^-$ (**2**, red); (c) $S_2P(p\text{-}CF_3C_6H_4)_2^-$ (**3**, purple); and (d) $S_2P(m\text{-}CF_3C_6H_4)_2^-$ (**4**, green). The colors of the bars represent the symmetry labels of the antibonding MOs participating in the transitions: a_1 (black), a_2 (green), b_1 (red), and b_2 (blue).

calculations are consistent with the additional high-energy feature that was modeled in the experimental curve fits for **5**–**7** (Figures 3e and 4).

To provide further evidence that the spectral differences result from molecular structure and symmetry relationships, TDDFT calculations were conducted on the aforementioned hypothetical molecular structure of the $S_2PPh_2^-$ anion in which the C_6H_5 groups were rotated to $\theta = 45.0°$ (**2a**). The rotated Ph groups in **2a** increase the resolution and intensity of the first pre-edge feature, as observed in the spectra of **5**–**7**. In addition, the peak positions in **2a** and **5**–**7**, all of which have the same symmetry, follow the electron-donating abilities of the aryl

dx.doi.org/10.1021/ja303999q | J. Am. Chem. Soc. 2012, 134, 14408–14422

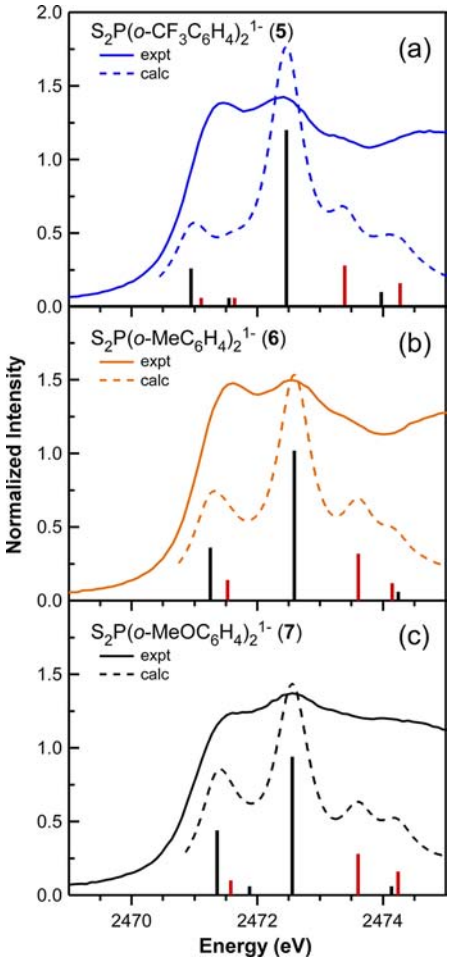

Figure 12. Sulfur K-edge X-ray absorption spectra (solid lines), TDDFT-simulated spectra (dotted lines), and calculated transitions (bars) for C_2-symmetric diaryldithiophosphinates: (a) $S_2P(o\text{-}CF_3C_6H_4)_2^-$ (**5**, blue); (b) $S_2P(o\text{-}MeC_6H_4)_2^-$ (**6**, orange); and (c) $S_2P(o\text{-}MeOC_6H_4)_2^-$ (**7**, black). The colors of the bars represent the symmetry labels of the antibonding MOs participating in the transitions: a (black) and b (red).

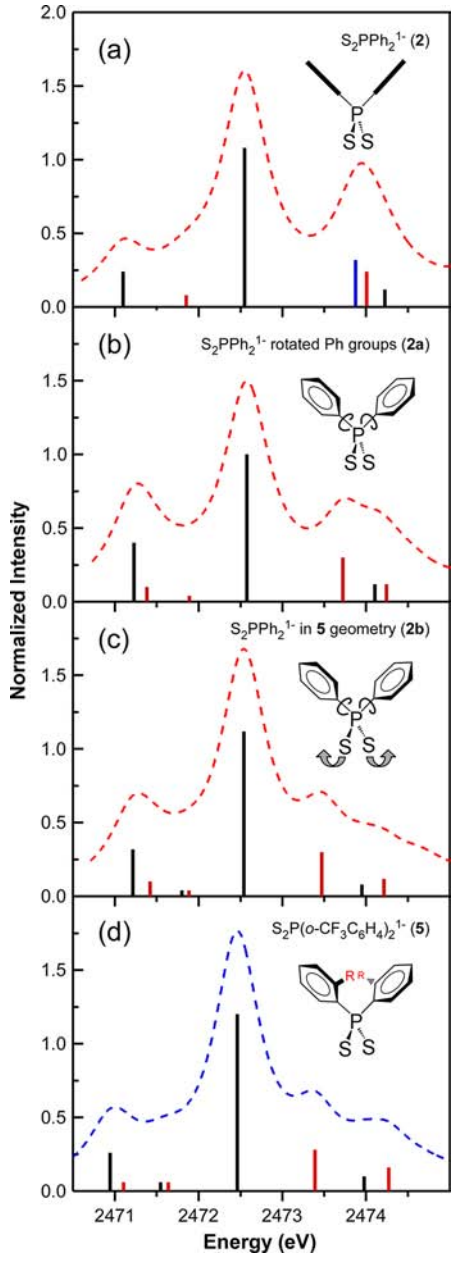

Figure 13. TDDFT-simulated sulfur K-edge X-ray absorption spectra (dotted lines) and calculated transitions (bars) for (a) $S_2PPh_2^-$ (**2**), (b) $S_2PPh_2^-$ with $\theta = 45°$ (**2a**), (c) $S_2PPh_2^-$ constrained in the $S_2P(o\text{-}CF_3C_6H_4)_2^-$ geometry (**2b**), and (d) $S_2P(o\text{-}CF_3C_6H_4)_2^-$ (**5**). The colors of the bars represent the symmetry labels of the antibonding MOs participating in the transitions: a or a_1 (black), b or b_1 (red), and b_2 (blue).

groups: **5** (o-CF_3) < **2a** (rotated phenyl groups) < **6** (o-Me) < **7** (o-MeO). Aside from the similarities in the first feature of **2a** compared to those in **5**–**7**, the associated transitions identified in the calculations for **2a** are similar to those for **6** and **7** but are slightly different from those in **5** (Figures 12 and 13b).

Additional TDDFT calculations on a second hypothetical structure of $S_2PPh_2^-$ showed transitions and a simulated spectrum almost identical to those of **5** (Figure 13). These calculations were performed using **2b**, a $S_2PPh_2^-$ structure that was constrained to be an exact match of $S_2P(o\text{-}CF_3C_6H_4)_2^-$ (**5**), including both rotated Ph groups (θ = 45.2°) and a distorted S_2PC_2 core with S–P–C angles equal to those observed for **5** (104.2° and 109.8°; Table 2). In the spectrum of **2b**, the relative energies and intensities for the low- and high-energy transitions match those calculated for **5**. These results suggest that when considering ancillary group effects on the electronic structure of $S_2PR_2^-$, both the aryl group orientation (indicated by θ) and slight variations of the S–P–C angles need to be considered.

In summary, the dramatic changes in the simulated sulfur K-edge XAS spectra of **2**, **2a**, and **2b** suggest that the key differences observed in the spectra of **2**–**4** compared with **5**–**7** stem primarily from the fact that the ortho substituents force a structural change that decreases the molecular symmetry from C_{2v} in **2**–**4** to C_2 in **5**–**7**. In turn, analysis of the TDDFT calculations complements the DFT results described above, which show that the symmetry change provides increased symmetry-allowed mixing between the b orbitals in **5**–**7** that are derived from the b_1 and b_2 orbitals in **2**–**4**. This appears to account in large part for the splitting of the b_1 and b_2 transitions under the third feature at ca. 2474 eV in **2**–**4** to their positions in **5**–**7** (Figure 11–13). Additional splitting of this feature is attributed to the nonuniform C–P–S angles, as observed in **2b** and **5** (Figure 13). The changes in symmetry and molecular

dx.doi.org/10.1021/ja303999q | J. Am. Chem. Soc. 2012, 134, 14408–14422

structure provide greater mixing between the sulfur atoms and the aryl π orbitals, which is responsible for a large intensity increase in the first sulfur K-edge XAS feature and the overall spectral differences observed for **5**−**7** compared with **2**−**4**.

Aryl Substituent Contributions to the Sulfur K-Edge XAS Spectra. While differences in the orientation of the aryl groups reflect dramatic differences in the sulfur K-edge XAS spectra of **2**−**4** compared with **5**−**7**, changes in the electronic structure due to the donor substituents are more subtle. For the CF_3-substituted **2**−**4**, the electron-donating effects are most easily identified by comparing the energies of the calculated 1s → $5a_1$ and 1s → $5b_1$ transitions and the experimental peak positions of the corresponding first pre-edge peaks. For example, for **2**−**4** (Figure 11b−d), the calculated energies of the transitions under the first pre-edge feature decrease slightly with increased electron-withdrawing capability of the aryl group [**2** (R = Ph) > **4** (R = *m*-$CF_3C_6H_4$) > **3** (R = *p*-$CF_3C_6H_4$)]: the transitions for **2**, with no CF_3 substituents, are higher in energy than those for **4** (whose *m*-CF_3 substituent withdraws electron density at the ortho position), while the transitions for **3** are lowest in energy (the *p*-CF_3 substituent withdraws electron density at the carbon directly attached to phosphorus).

In comparison with the spectra of **2**−**4**, the differences in the energies of the transitions in **5**−**7** are more pronounced, which appears to be a consequence of the diverse donor properties of CF_3, Me, and MeO. The energies of the calculated 1s → 7a and 1s → 8b transitions under the first feature increase in the order **7** (MeO) < **6** (Me) < **5** (CF_3) (Figure 12), which is consistent with the trend in the donor strengths of the strongly donating (MeO), weakly donating (Me), and electron-withdrawing (CF_3) substituents. This trend is consistent with the experimental data, as the rising edge position for the first peak decreases in energy in going from **7** (*o*-MeO) to **6** (*o*-Me) and is almost indistinguishable for **6** (*o*-Me) and **5** (*o*-CF_3) (Figure 2c). Hence, the calculations indicate that as donation of electron density into the MOs containing sulfur 3p character decreases, the energy associated with transitions for the first pre-edge feature in the sulfur K-edge XAS spectrum decreases, as is observed experimentally. The correlation between the electron-withdrawing ability of the ancillary groups attached to phosphorus and the energy of the first pre-edge feature for all of the aryl-containing compounds (**2**−**7**) is also consistent with the previously reported ^{31}P NMR spectra, which show that the resonances shift to higher field as the electron density on the phosphorus nucleus increases.[73]

■ CONCLUSION AND OUTLOOK

The term "soft-donor" extractant is used collectively to refer to extractants that exhibit selectivity for minor actinides. The term arises primarily from empirical data obtained from the screening of organic extractants in minor actinide extraction studies. Within the context of hard/soft acid−base theory, the vast majority of extractants that exhibit selectivity for minor actinides contain donor atoms that are considered to be softer bases than oxygen (N, S, Cl). Hence, as the name implies, it is assumed that ligand softness is important for directing effective separations. While there are remarkable trends in minor actinide selectivity in comparisons of otherwise identical ligands containing donor atoms of varying softness [e.g., $S_2P(o\text{-}CF_3C_6H_4)_2^-$ (SF = 100 000)[71] vs $O_2P(o\text{-}CF_3C_6H_4)_2^-$ (SF = 0.01)[72]], it is not clear whether the trend relating ligand softness and selectivity holds in comparisons among a series of ligands containing identical soft-donor atoms. In this study, we have demonstrated that ligand K-edge XAS and TDDFT can be used to quantify electronic structure variations that relate to ligand softness, and we have shown that the special electronic properties observed for $S_2P(o\text{-}CF_3C_6H_4)_2^-$ correlate with its exceptionally high minor actinide selectivity.

We have measured and evaluated two interrelated electronic properties that reflect ligand softness: ligand polarizability and the energy of the highest occupied MO (HOMO).[77] In general, softer ligands are considered to be more polarizable and delocalize electron density more efficiently over the entire ligand. This is consistent with the sulfur K-edge XAS results, which show that rotation of the arene rings in ortho-substituted diaryldithiophosphinates allows greater delocalization of electron density on sulfur into the arene π orbitals, as reflected by the large increase in first peak intensity in the spectra of **5**−**7** compared with **2**−**4**. The DFT calculations clearly indicate that increased delocalization and the reduction in symmetry from C_{2v} in **2**−**4** to C_2 in **5**−**7** result in a substantial increase in the energy of their highest MOs (Figure 8). The electronic structure variations of diaryldithiophosphinates as they relate to ligand softness are consistent with the observed minor actinide selectivity differences between the C_2-symmetric anion $S_2P(o\text{-}CF_3C_6H_4)_2^-$ in **5** (high selectivity) and the C_{2v} anion $S_2P(m\text{-}CF_3C_6H_4)_2^-$ in **4** (moderate selectivity). The ortho substitution in **5** inhibits rotation of the aryl groups into C_{2v} symmetry, thereby holding the $S_2P(o\text{-}CF_3C_6H_4)_2^-$ ion in a geometric configuration that appears electronically poised for higher actinide binding selectivity. In this sense, the $S_2P(o\text{-}CF_3C_6H_4)_2^{1-}$ anion could be described as being in an "entatic state," a concept of a geometric or electronic condition that is adapted for a given function (in this case, binding selectivity).[78]

We have found that the MOs used to form metal−sulfur σ bonds upon metal binding (namely, the HOMO in $S_2PR_2^-$) are heavily influenced by the presence of ortho substituents on the arene ring, regardless of their electron-withdrawing (CF_3) or electron-donating (Me and OMe) properties. Hence, it is tempting to propose **6** and **7** should be effective actinide extractants as well. However, we caution that varying the identity of the arene ring substituents affects other properties that are critical to effective separations. For example, although addition of Me and MeO aryl substituents in **6** and **7** may provide selectivity for binding actinides over lanthanides, it also dramatically decreases the solubility of their acids in nonpolar solvents compared with $HS_2P(o\text{-}CF_3C_6H_4)_2$.[73] The decreased solubility could have deleterious consequences on their ability to extract actinides from aqueous media into organic diluents effectively.

The results presented here demonstrate that ligand K-edge XAS combined with DFT calculations can be used to correlate electronic structure and bonding with the selectivity for extracting minor actinides from lanthanides. By analyzing a series of effective and ineffective dithiophosphinate extractants, we have provided evidence that unique bonding features associated with effective extractants can be identified while avoiding the hazards associated with handling highly radioactive americium and curium analytes. Current efforts are focused on determining whether the conclusions based on the solid-state data presented here are also supported by solution-phase sulfur K-edge XAS measurements.[79−81] In addition, these results provide the foundation for distinguishing sulfur K-edge XAS transitions attributed to P−S ligand bonding from transitions associated with metal−sulfur interactions, which is essential for the analyses of $M(S_2PR_2)_x^{(3-x)}$ complexes (M = trivalent minor

actinide or lanthanide) that are currently in progress. Overall, these sulfur K-edge XAS and TDDFT results provide valuable insight into structure/function relationships in dithiophosphinate extractants, which can be used for future innovation in minor actinide extraction chemistry to support the development of advanced nuclear fuel cycles.

EXPERIMENTAL SECTION

General Considerations. The tetraphenylphosphonium dithiophosphinate salts **1**−**7** were prepared as previously described.[73] Toluene was dried using sodium and benzophenone, vacuum-distilled, and degassed by three freeze−pump−thaw cycles before use. Polystyrene (PolySciences Inc.) was acquired as 3.0 Micron Dry Form and dried under vacuum (10^{-3} Torr) for 24 h. $Na_2S_2O_3$ was acquired from Fisher and treated similarly.

XAS Sample Preparation. The XAS samples were prepared in a He-filled glovebox by finely grinding the analyte (7−10 mg) with polystyrene beads (120 mg) for 2 min in a Wig-L-Bug grinder to obtain a homogeneous mixture. An aliquot of this mixture was transferred to a vial, and polystyrene was added, giving a total mass of the final mixture of 90 mg and a sulfur concentration of 6×10^{-5} mmol of S/mg. The new mixture was ground for 2 min in the Wig-L-Bug grinder to achieve small and finely divided particles. An aliquot of this mixture (60 mg) was transferred to a vial, and toluene (0.4 mL) was added. The resulting solution was transferred to a 5 mm × 11 mm × 4 mm well in an aluminum sample plate that had been secured to a Teflon block. After 48 h, the toluene had evaporated, and the Teflon plate was removed, leaving a robust film fixed in the sample-plate window.

Sulfur K-edge XAS Measurements. All of the data were collected at the Stanford Synchrotron Radiation Lightsource under dedicated operating conditions of 3.0 GeV and 300 mA. Data were measured using the 54-pole wiggler beamline 6-2 with a Ni-coated harmonic rejection mirror and a Si(111) double-crystal monochromator detuned by 50% (3150 eV). The spectra were collected at room temperature under vacuum (10^{-6}) using a chamber similar to that described previously.[69] The sample excitation fluorescence was measured against the incident beam using pairs of backward-facing International Radiation Detector XUV100-type photodiodes coated with 1000 Å of aluminum. The incident beam intensity was measured as the scatter from a polypropylene window using an identically configured photodiode pair. The energy was calibrated to 2472.02 eV using the maximum of the first pre-edge feature in the sulfur K-edge X-ray absorption spectrum of the $Na_2S_2O_3$ standard,[68] which was repeatedly analyzed between sample scans.

Sulfur K-edge XAS Data Analysis. A first-order polynomial was fit to the pre-edge region (2375−2465 eV) and then subtracted from the experimental data to eliminate the background of the spectrum. The data were normalized by fitting a third-order polynomial to the post-edge region of the spectra (2510−2690 eV) and setting the step function at 2490 eV to an intensity of 1.0. Fits to the sulfur K-edges were performed using the program IGOR 6.0 and a modified version of EDG_FIT.[68] First- and second-derivative spectra were used as guides to determine the number and positions of peaks. Pre-edge and rising-edge features were modeled by pseudo-Voigt line shapes and a step function. For the pre-edge and white-line features, a fixed 1:1 ratio of Lorentzian and Gaussian contributions was used, and for the step function, a 1:1 ratio of arctangent and error function contributions was employed. Fits were performed over several energy ranges. Experimental peak positions were determined by identifying minima in second-derivative traces.

Ground-State DFT Calculations. Ground-state electronic structure calculations for all species were performed using restricted DFT in the Gaussian 09 code.[82] The hybrid B3LYP functional employed used Becke's three-parameter exchange functional (B3)[83] along with the correlation functional of Lee, Yang, and Parr (LYP).[84] All atoms were modeled using an all-electron Pople-style double-ζ 6-31G(d′,p′) basis set with polarization functions optimized for heavy atoms.[85,86] These functionals and basis sets have previously been shown to reproduce selectivity factors for Am and Eu with dithiophosphinate ligands.[87] The populations of the sulfur 3p orbitals in each compound were then obtained by Mulliken population analysis of individual MOs.

TDDFT Calculations. The sulfur K-edge XAS spectra were simulated using TDDFT. These calculations were conducted as previously described,[58,69,70,88] and involved evaluating core electron excitations by exploiting the small amount of mixing between the core orbitals and the high-lying unoccupied virtual orbitals. Specifically, this analysis involved a linear response calculation to extract the probability amplitudes from the transition densities and dipole moments between the calculated excited states and the ground states.[89] The excitations originating from all of the intermediate states between the sulfur 1s orbitals and the HOMO were excluded so that only excitations from the core levels to virtual MOs could be analyzed. This allowed the virtual orbitals to mix with one another to reflect, at least to first order, the presence of the core hole on sulfur. Relaxations in the occupied orbitals other than the sulfur 1s orbitals were not included. Although excluding orbital relaxations in the occupied orbitals affects the absolute transition energies, the relative excitation energies are more reliable. In fact, previous calculations on transition-metal compounds have provided very good agreement with experimental measurements.[58,69,70,88] A shift of +57.4 eV was added to the calculated spectra to account for omission of the atomic relaxation associated with the core excitation, relativistic stabilization, and errors associated with the functional.

ASSOCIATED CONTENT

Supporting Information

Complete sulfur K-edge XAS data and curve-fitting models for compounds **1**−**7**, calculated atomic coordinates, Mulliken charges, and complete ref 82. This material is available free of charge via the Internet at http://pubs.acs.org.

AUTHOR INFORMATION

Corresponding Author

stosh@lanl.gov

Notes

The authors declare no competing financial interest.

ACKNOWLEDGMENTS

We thank Professor Bruce Bursten and Dr. Dean Peterman for helpful discussions. This work was supported by U.S. Department of Energy, Office of Basic Energy Sciences, Division of Chemical Sciences, Geosciences, and Biosciences (Heavy Element Chemistry Program), the U.S. Department of Energy, Office of Nuclear Energy (Fuel Cycle R&D Program), a Glenn T. Seaborg Institute Postdoctoral Fellowship (S.R.D.), and a LANL Director's Postdoctoral Fellowship (J.M.K.). Portions of this research were carried out at the Stanford Synchrotron Radiation Lightsource (SSRL), a national user facility supported by the U.S. Department of Energy, Office of Basic Energy Sciences. Los Alamos National Laboratory is operated by Los Alamos National Security, LLC, for the National Nuclear Security Administration of the U.S. Department of Energy under Contract DEAC52-06NA25396.

REFERENCES

(1) Choppin, G. R. *J. Less-Common Met.* **1983**, *93*, 323−330.
(2) Nash, K. L. *Solvent Extr. Ion Exch.* **1993**, *11*, 729−768.
(3) Nilsson, M.; Nash, K. L. *Solvent Extr. Ion Exch.* **2007**, *25*, 665−701.
(4) Braley, J. C.; Grimes, T. S.; Nash, K. L. *Ind. Eng. Chem. Res.* **2012**, *51*, 627−636.

(5) Smith, B. F.; Jarvinen, G. D.; Jones, M. M.; Hay, P. J. *Solvent Extr. Ion Exch.* **1989**, *7*, 749−765.
(6) Zhu, Y.; Chen, J.; Choppin, G. R. *Solvent Extr. Ion Exch.* **1996**, *14*, 543−553.
(7) Zhu, Y.; Chen, J.; Jiao, R. *Solvent Extr. Ion Exch.* **1996**, *14*, 61−68.
(8) Kolarik, Z.; Muellich, U. *Solvent Extr. Ion Exch.* **1997**, *15*, 361−379.
(9) Hill, C.; Madic, C.; Baron, P.; Ozawa, M.; Tanaka, Y. *J. Alloys Compd.* **1998**, *271*−*273*, 159−162.
(10) Modolo, G.; Odoj, R. *J. Alloys Compd.* **1998**, *271*−*273*, 248−251.
(11) Watanabe, M.; Mirvaliev, R.; Tachimori, S.; Takeshita, K.; Nakano, Y.; Morikawa, K.; Chikazawa, T.; Mori, R. *Solvent Extr. Ion Exch.* **2004**, *22*, 377−390.
(12) Bhattacharyya, A.; Mohapatra, P. K.; Manchanda, V. K. *Solvent Extr. Ion Exch.* **2007**, *25*, 27−39.
(13) Dam, H. H.; Reinhoudt, D. N.; Verboom, W. *Chem. Soc. Rev.* **2007**, *36*, 367−377.
(14) Kolarik, Z. *Chem. Rev.* **2008**, *108*, 4208−4252.
(15) Xu, Q.; Wu, J.; Chang, Y.; Zhang, L.; Yang, Y. *Radiochim. Acta* **2008**, *96*, 771−779.
(16) Lumetta, G. J.; Gelis, A. V.; Vandegrift, G. F. *Solvent Extr. Ion Exch.* **2010**, *28*, 287−312.
(17) Modolo, G.; Kluxen, P.; Geist, A. *Radiochim. Acta* **2010**, *98*, 193−201.
(18) Lewis, F. W.; Harwood, L. M.; Hudson, M. J.; Drew, M. G. B.; Desreux, J. F.; Vidick, G.; Bouslimani, N.; Modolo, G.; Wilden, A.; Sypula, M.; Vu, T.-H.; Simonin, J.-P. *J. Am. Chem. Soc.* **2011**, *133*, 13093−13102.
(19) Ozcubukcu, S.; Mandal, K.; Wegner, S.; Jensen, M. P.; He, C. *Inorg. Chem.* **2011**, *50*, 7937−7939.
(20) *Solvent Extraction Principles and Practice*, 2nd revised and expanded ed.; Rydberg, J., Cox, M., Musikas, C., Choppin, G. R., Eds.; Marcel Dekker: New York, 2004.
(21) Diamond, R. M.; Street, K., Jr.; Seaborg, G. T. *J. Am. Chem. Soc.* **1954**, *76*, 1461−1469.
(22) Jensen, M. P.; Bond, A. H. *J. Am. Chem. Soc.* **2002**, *124*, 9870−9877.
(23) Smith, H. L.; Hoffman, D. C. *J. Inorg. Nucl. Chem.* **1956**, *3*, 243−247.
(24) Surls, J. P., Jr.; Choppin, G. R. *J. Inorg. Nucl. Chem.* **1957**, *4*, 62−73.
(25) Chiarizia, R.; Danesi, P. R.; Scibona, G.; Magon, L. *J. Inorg. Nucl. Chem* **1973**, *35*, 3595−3604.
(26) Svantesson, I.; Hangstroem, I.; Persson, G.; Liljenzin, J. O. *Radiochem. Radioanal. Lett.* **1979**, *37*, 215−222.
(27) Danesi, P. R.; Chiarizia, R.; Rickert, P.; Horwitz, E. P. *Solvent Extr. Ion Exch.* **1985**, *3*, 111−147.
(28) Brigham, D.; Badajoz, C.; Cote, G.; Nash, K. L. *Solvent Extr. Ion Exch.* **2011**, *29*, 270−291.
(29) Hedman, B.; Frank, P.; Gheller, S. F.; Roe, A. L.; Newton, W. E.; Hodgson, K. O. *J. Am. Chem. Soc.* **1988**, *110*, 3798−3805.
(30) Hedman, B.; Hodgson, K. O.; Solomon, E. I. *J. Am. Chem. Soc.* **1990**, *112*, 1643−1645.
(31) Shadle, S. E.; Penner-Hahn, J. E.; Schugar, H. J.; Hedman, B.; Hodgson, K. O.; Solomon, E. I. *J. Am. Chem. Soc.* **1993**, *115*, 767−776.
(32) Mueller, A.; Wittneben, V.; Diemann, E.; Hormes, J.; Kuetgens, U. *Chem. Phys. Lett.* **1994**, *225*, 359−363.
(33) Shadle, S. E.; Hedman, B.; Hodgson, K. O.; Solomon, E. I. *Inorg. Chem.* **1994**, *33*, 4235−4244.
(34) Shadle, S. E.; Hedman, B.; Hodgson, K. O.; Solomon, E. I. *J. Am. Chem. Soc.* **1995**, *117*, 2259−2272.
(35) Gamelin, D. R.; Williams, K. R.; LaCroix, L. B.; Houser, R. P.; Tolman, W. B.; Mulder, T. C.; de Vries, S.; Hedman, B.; Hodgson, K. O.; Solomon, E. I. *J. Am. Chem. Soc.* **1997**, *119*, 613−614.
(36) Williams, K. R.; Hedman, B.; Hodgson, K. O.; Solomon, E. I. *Inorg. Chim. Acta* **1997**, *263*, 315−321.
(37) Rose, K.; Shadle, S. E.; Eidsness, M. K.; Kurtz, D. M., Jr.; Scott, R. A.; Hedman, B.; Hodgson, K. O.; Solomon, E. I. *J. Am. Chem. Soc.* **1998**, *120*, 10743−10747.
(38) Izumi, Y.; Glaser, T.; Rose, K.; McMaster, J.; Basu, P.; Enemark, J. H.; Hedman, B.; Hodgson, K. O.; Solomon, E. I. *J. Am. Chem. Soc.* **1999**, *121*, 10035−10046.
(39) Rose, K.; Shadle, S. E.; Glaser, T.; de Vries, S.; Cherepanov, A.; Canters, G. W.; Hedman, B.; Hodgson, K. O.; Solomon, E. I. *J. Am. Chem. Soc.* **1999**, *121*, 2353−2363.
(40) Anxolabehere-Mallart, E.; Glaser, T.; Frank, P.; Aliverti, A.; Zanetti, G.; Hedman, B.; Hodgson, K. O.; Solomon, E. I. *J. Am. Chem. Soc.* **2001**, *123*, 5444−5452.
(41) Glaser, T.; Rose, K.; Shadle, S. E.; Hedman, B.; Hodgson, K. O.; Solomon, E. I. *J. Am. Chem. Soc.* **2001**, *123*, 442−454.
(42) Szilagyi, R. K.; Lim, B. S.; Glaser, T.; Holm, R. H.; Hedman, B.; Hodgson, K. O.; Solomon, E. I. *J. Am. Chem. Soc.* **2003**, *125*, 9158−9169.
(43) Dey, A.; Glaser, T.; Couture, M. M. J.; Eltis, L. D.; Holm, R. H.; Hedman, B.; Hodgson, K. O.; Solomon, E. I. *J. Am. Chem. Soc.* **2004**, *126*, 8320−8328.
(44) Dey, A.; Glaser, T.; Moura, J. J. G.; Holm, R. H.; Hedman, B.; Hodgson, K. O.; Solomon, E. I. *J. Am. Chem. Soc.* **2004**, *126*, 16868−16878.
(45) Szilagyi, R. K.; Bryngelson, P. A.; Maroney, M. J.; Hedman, B.; Hodgson, K. O.; Solomon, E. I. *J. Am. Chem. Soc.* **2004**, *126*, 3018−3019.
(46) Dey, A.; Okamura, T.; Ueyama, N.; Hedman, B.; Hodgson, K. O.; Solomon, E. I. *J. Am. Chem. Soc.* **2005**, *127*, 12046−12053.
(47) DeBeer George, S.; Brant, P.; Solomon Edward, I. *J. Am. Chem. Soc.* **2005**, *127*, 667−674.
(48) DeBeer George, S.; Huang, K.-W.; Waymouth, R. M.; Solomon, E. I. *Inorg. Chem.* **2006**, *45*, 4468−4477.
(49) Dey, A.; Chow, M.; Taniguchi, K.; Lugo-Mas, P.; Davin, S.; Maeda, M.; Kovacs, J. A.; Odaka, M.; Hodgson, K. O.; Hedman, B.; Solomon, E. I. *J. Am. Chem. Soc.* **2006**, *128*, 533−541.
(50) Dey, A.; Hocking, R. K.; Larsen, P.; Borovik, A. S.; Hodgson, K. O.; Hedman, B.; Solomon, E. I. *J. Am. Chem. Soc.* **2006**, *128*, 9825−9833.
(51) Dey, A.; Green, K. N.; Jenkins, R. M.; Jeffrey, S. P.; Darensbourg, M.; Hodgson, K. O.; Hedman, B.; Solomon, E. I. *Inorg. Chem.* **2007**, *46*, 9655−9660.
(52) Dey, A.; Jeffrey, S. P.; Darensbourg, M.; Hodgson, K. O.; Hedman, B.; Solomon, E. I. *Inorg. Chem.* **2007**, *46*, 4989−4996.
(53) Dey, A.; Jenney, F. E., Jr.; Adams, M. W. W.; Johnson, M. K.; Hodgson, K. O.; Hedman, B.; Solomon, E. I. *J. Am. Chem. Soc.* **2007**, *129*, 12418−12431.
(54) Kapre Ruta, R.; Bothe, E.; Weyhermuller, T.; DeBeer George, S.; Muresan, N.; Wieghardt, K. *Inorg. Chem.* **2007**, *46*, 7827−7839.
(55) Ray, K.; DeBeer George, S.; Solomon, E. I.; Wieghardt, K.; Neese, F. *Chem.—Eur. J.* **2007**, *13*, 2783−2797.
(56) Sarangi, R.; DeBeer George, S.; Rudd, D. J.; Szilagyi, R. K.; Ribas, X.; Rovira, C.; Almeida, M.; Hodgson, K. O.; Hedman, B.; Solomon, E. I. *J. Am. Chem. Soc.* **2007**, *129*, 2316−2326.
(57) Tenderholt, A. L.; Szilagyi, R. K.; Holm, R. H.; Hodgson, K. O.; Hedman, B.; Solomon, E. I. *J. Inorg. Biochem.* **2007**, *101*, 1594−1600.
(58) Kozimor, S. A.; Yang, P.; Batista, E. R.; Boland, K. S.; Burns, C. J.; Christensen, C. N.; Clark, D. L.; Conradson, S. D.; Hay, P. J.; Lezama, J. S.; Martin, R. L.; Schwarz, D. E.; Wilkerson, M. P.; Wolfsberg, L. E. *Inorg. Chem.* **2008**, *47*, 5365−5371.
(59) Sarangi, R.; York, J. T.; Helton, M. E.; Fujisawa, K.; Karlin, K. D.; Tolman, W. B.; Hodgson, K. O.; Hedman, B.; Solomon, E. I. *J. Am. Chem. Soc.* **2008**, *130*, 676−686.
(60) Tenderholt, A. L.; Szilagyi, R. K.; Holm, R. H.; Hodgson, K. O.; Hedman, B.; Solomon, E. I. *Inorg. Chem.* **2008**, *47*, 6382−6392.
(61) Dey, A.; Jiang, Y.; Ortiz de Montellano, P.; Hodgson, K. O.; Hedman, B.; Solomon, E. I. *J. Am. Chem. Soc.* **2009**, *131*, 7869−7878.
(62) Milsmann, C.; Sproules, S.; Bill, E.; Weyhermueller, T.; DeBeer George, S.; Wieghardt, K. *Chem.—Eur. J.* **2010**, *16*, 3628−3645.

(63) Tenderholt, A. L.; Wang, J.-J.; Szilagyi, R. K.; Holm, R. H.; Hodgson, K. O.; Hedman, B.; Solomon, E. I. *J. Am. Chem. Soc.* **2010**, *132*, 8359−8371.
(64) Dey, A.; Peng, Y.; Broderick, W. E.; Hedman, B.; Hodgson, K. O.; Broderick, J. B.; Solomon, E. I. *J. Am. Chem. Soc.* **2011**, *133*, 18656−18662.
(65) Sarangi, R.; Yang, L.; Winikoff, S. G.; Gagliardi, L.; Cramer, C. J.; Tolman, W. B.; Solomon, E. I. *J. Am. Chem. Soc.* **2011**, *133*, 17180−17191.
(66) Sun, N.; Liu, L. V.; Dey, A.; Villar-Acevedo, G.; Kovacs, J. A.; Darensbourg, M. Y.; Hodgson, K. O.; Hedman, B.; Solomon, E. I. *Inorg. Chem.* **2011**, *50*, 427−436.
(67) Glaser, T.; Hedman, B.; Hodgson, K. O.; Solomon, E. I. *Acc. Chem. Res.* **2000**, *33*, 859−868.
(68) Solomon, E. I.; Hedman, B.; Hodgson, K. O.; Dey, A.; Szilagyi, R. K. *Coord. Chem. Rev.* **2005**, *249*, 97−129.
(69) Kozimor, S. A.; Yang, P.; Batista, E. R.; Boland, K. S.; Burns, C. J.; Clark, D. L.; Conradson, S. D.; Martin, R. L.; Wilkerson, M. P.; Wolfsberg, L. E. *J. Am. Chem. Soc.* **2009**, *131*, 12125−12136.
(70) Minasian, S. G.; Keith, J. M.; Batista, E. R.; Boland, K. S.; Christensen, C. N.; Clark, D. L.; Conradson, S. D.; Kozimor, S. A.; Martin, R. L.; Schwarz, D. E.; Shuh, D. K.; Wagner, G. L.; Wilkerson, M. P.; Wolfsberg, L. E.; Yang, P. *J. Am. Chem. Soc.* **2012**, *134*, 5585−5597.
(71) Klaehn, J. R.; Peterman, D. R.; Harrup, M. K.; Tillotson, R. D.; Luther, T. A.; Law, J. D.; Daniels, L. M. *Inorg. Chim. Acta* **2008**, *361*, 2522−2532.
(72) Peterman, D. R.; Greenhalgh, M. R.; Tillotson, R. D.; Klaehn, J. R.; Harrup, M. K.; Luther, T. A.; Law, J. D. *Sep. Sci. Technol.* **2010**, *45*, 1711−1717.
(73) Daly, S. R.; Klaehn, J. R.; Boland, K. S.; Kozimor, S. A.; MacInnes, M. M.; Peterman, D. R.; Scott, B. L. *Dalton Trans.* **2012**, *41*, 2163−2175.
(74) Benson, M. T.; Moser, M. L.; Peterman, D. R.; Dinescu, A. *THEOCHEM* **2008**, *867*, 71−77.
(75) Leavitt, C. M.; Gresham, G. L.; Benson, M. T.; Gaumet, J.-J.; Peterman, D. R.; Klaehn, J. R.; Moser, M.; Aubriet, F.; Van Stipdonk, M. J.; Groenewold, G. S. *Inorg. Chem.* **2008**, *47*, 3056−3064.
(76) Albright, T. A.; Burdett, J. K.; Whangbo, M. *Orbital Interactions in Chemistry*; Wiley: New York, 1985.
(77) Minkin, V. I. *Pure Appl. Chem.* **1999**, *71*, 1919−1981.
(78) Vallee, B. L.; Williams, R. J. P. *Proc. Natl. Acad. Sci. U.S.A.* **1968**, *59*, 498−505.
(79) Sun, N.; Dey, A.; Xiao, Z.; Wedd, A. G.; Hodgson, K. O.; Hedman, B.; Solomon, E. I. *J. Am. Chem. Soc.* **2010**, *132*, 12639−12647.
(80) Sarangi, R.; Gorelsky, S. I.; Basumallick, L.; Hwang, H. J.; Pratt, R. C.; Stack, T. D. P.; Lu, Y.; Hodgson, K. O.; Hedman, B.; Solomon, E. I. *J. Am. Chem. Soc.* **2008**, *130*, 3866−3877.
(81) Basumallick, L.; Sarangi, R.; DeBeer George, S.; Elmore, B.; Hooper, A. B.; Hedman, B.; Hodgson, K. O.; Solomon, E. I. *J. Am. Chem. Soc.* **2005**, *127*, 3531−3544.
(82) Frisch, M. J.; et al. *Gaussian 09*, revision B.01; Gaussian, Inc.: Wallingford, CT, 2009.
(83) Becke, A. D. *J. Chem. Phys.* **1993**, *98*, 5648−5652.
(84) Lee, C.; Yang, W.; Parr, R. G. *Phys. Rev. B* **1988**, *37*, 785−789.
(85) Petersson, G. A.; Bennett, A.; Tensfeldt, T. G.; Al-Laham, M. A.; Shirley, W. A.; Mantzaris, J. *J. Chem. Phys.* **1988**, *89*, 2193−2218.
(86) Petersson, G. A.; Al-Laham, M. A. *J. Chem. Phys.* **1991**, *94*, 6081−6090.
(87) Keith, J. M.; Batista, E. R. *Inorg. Chem.* **2012**, *51*, 13−15.
(88) Bradley, J. A.; Yang, P.; Batista, E. R.; Boland, K. S.; Burns, C. J.; Clark, D. L.; Conradson, S. D.; Kozimor, S. A.; Martin, R. L.; Seidler, G. T.; Scott, B. L.; Shuh, D. K.; Tyliszczak, T.; Wilkerson, M. P.; Wolfsberg, L. E. *J. Am. Chem. Soc.* **2010**, *132*, 13914−13921.
(89) Elliott, P.; Furche, F.; Burke, K. *Rev. Comput. Chem.* **2009**, *26*, 91−165.